文章编号：1001-9014(2020)03-0279-05

DOI:10. 11972/j. issn. 1001-9014. 2020. 03. 002

CMOS compatible multichannel mid-infrared photonic crystal sensor

ZHOU Yi*, WANG Lei, LI Jun, YANG Xue-Lei, GAN Feng-Yuan, ZHAO Ying-Xuan, QIU Chao, LI Wei

(Laboratory of Silicon based Materials and Integrated Devices, Shanghai Institute of Microsystem and Information Technology, Chinese Academy of Sciences, Shanghai 200050, China)

Abstract: We propose a multichannel two-dimensional optical chemical sensor in a photonic crystal (PhC) slab. The device is composed of four cavities with a center wavelength at 3. 3μm, and the channels are spaced by 10nm. The sensor is designed on an 800-nm-thick silicon-on-insulator platform for standard CMOS technology. The optical characteristics of the nanocavity structure are simulated by 3-D finite difference time-domain (FDTD) method. The transmittance of each channel is about 39%, with non-uniformity of transmittance across channels less than 0. 25dB. The capability of the sensor is demonstrated by detecting carbon tetrachloride and benzene solutions, and shows a sensitivity of 209. 2nm/RIU.

Key words: photonic crystal, sensor, multichannel, mid-infrared

PACS: 07. 07. Df Sensors, 42. 70. Qs Photonic bandgap materials, 42. 82. Gw Other integrated optical elements and systems

CMOS兼容的中红外多通道光子晶体传感器

周 易*, 王 磊, 李 军, 杨雪雷, 甘峰源, 赵瑛璇, 仇 超, 李 伟

(中国科学院上海微系统与信息技术研究所,硅基材料与集成器件实验室,上海 200050)

摘要:提出了一种基于光子晶体的二维多通道光学化学传感器。该器件由中心波长为3.3 μm的四个腔组成,各通道工作波长间隔为10 nm。该传感器采用800 nm厚的绝缘体上硅材料,可利用标准CMOS技术加工。通过三维时差有限差分法对微腔结构的光学特性进行模拟。每个通道的传输效率为39%,通道之间的传输效率不一致性小于0.25dB。该传感器的功能为检测四氯化碳和苯溶液浓度,其灵敏度为209.2 nm/RIU。

关 键 词:光子晶体;传感器;多通道;中红外

中图分类号:O799,O439 **文献标识码**:A

Introduction

In recent years, chemical and biological sensor arrays using photonic crystals have been vigorously studied because of their potential for nanophotonic label-free environmental monitoring and biomedical detection[1-2]. The mid-infrared wavelength range (2~20 μm) represents the characteristic absorption fingerprints of most molecules. For instance, aromatic C-H stretch, which is stable in structure, difficult to decompose, and highly toxic, has a strong absorption at λ = 3. 3 μm[3]. The silicon-on-insulator (SOI) structure with a 3~5 μm transmission window is an ideal material to design PhC sensor to detect aromatic compounds[4].

With photonic band gaps, PhC can afford us complete control over light propagation by preventing light from propagating in certain direction with specific frequencies. Nevertheless, the actual fabrication of a three-dimension periodic structure remains difficult. So PhC slabs using two-dimensional periodicity combined with vertical index-guiding are proposed. By introducing line and point defects in PhC slabs, one can create waveguides[5], cavities[6-7], bends[8-9], splitters[10] and filters[11-13] of compact size. Frequency-domain plane-wave expanded method is used for the solution of partial differential equations to find band structure ω(k) and the asso-

Received date: 2019- 11- 12, **revised date**: 2020- 02- 24 **收稿日期**:2019- 11- 12,**修回日期**:2020- 02- 24

Foundation items: Supported by the Shanghai Sailing Program (18YF1428200, 18YF1428100)

Biography: YI Zhou (1993-), female, Jiangshan, assistant professor, master. Research area involves micro/nanophotonics. E-mail: yizhou1012@mail. sim. ac. cn.

* **Corresponding author**: E-mail: yizhou1012@mail. sim. ac. cn

ciated fields for PhC[14]. The TE gaps for the triangular lattice of air holes are usually larger than those of the square lattice because the former is more symmetric, and the hexagonal Brullouin zone of the former is more circular. So the triangular lattice of air holes was chosen.

In this paper, we present a four-channel mid-infrared silicon PhC sensor working at λ = 3.3μm, spaced by 10nm. The sensor is designed on SOI platform for standard CMOS technique. The optical characteristics of the nanocavity structure are simulated by 3D-FDTD method. The transmittance of each channel is about 39%, with non-uniformity of transmittance across channels less than 0.25 dB. The capability of the sensor is demonstrated by detecting carbon tetrachloride and benzene solutions, and shows a sensitivity of 209.2 nm/RIU.

1 Design and Optimization of Sensor

The schematic of the designed multiport in-plane sensor is depicted in Fig. 1, which consists of a bus waveguide, drop waveguides, and cavities. Two 60° bend line defects are introduced into multichannel operation.

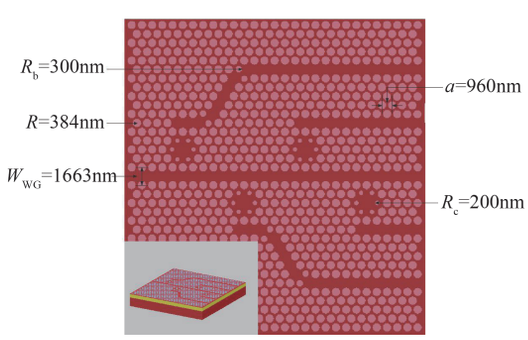

Fig. 1 Schematic structure of the designed multiport in-plane sensor
图1 多通道片上传感器的结构示意图

The band structure for a crystal consisting of air holes in silicon (ε = 11.792) with radius r = 0.4a is plotted in Fig. 2. There is a gap between the first and second TE bands, from $\omega a/2\pi c$ = 0.248 to $\omega a/2\pi c$ = 0.405 with the band width as 47.9%. There are light cones ($\omega \geqslant c|\mathbf{k}_{\parallel}|$) for the extended modes propagating in the air or SiO_2 substrate, where $\mathbf{k}_{\parallel}$ is the horizontal wave vector. As the light cone exists, we select our operating wavelength $\lambda = 2\pi c/\omega$ = 3.3μm to lie at frequency $\omega a/2\pi c$ = 0.291. So we can calculate the lattice constant as a = 960nm, and the air hole radius r = 0.4a = 384 nm. We set the thickness of slab as 800nm, which is thick enough for the fundamental mode to be well confined and thin enough to forbid higher-order modes to propagate within the slab.

A photonic crystal sensor is composed of a cavity and two waveguides, i. e. the bus waveguide and the drop waveguide. For multi-channel operation, two 60° bend line defects are introduced. We apply a simple optimization method, which makes the bend mode as symmetric as the straight waveguide mode[15]. The two air

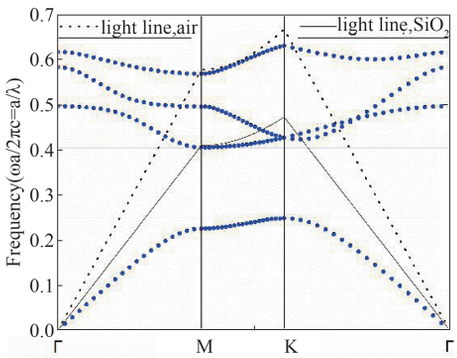

Fig. 2 Band diagram for the PhC slab.
图2 光子晶体能带图

holes at the corner are of radius R_b=300 nm, and they are shifted 50 nm away in opposite directions along the symmetric axis of the bend. The mechanism for improvement of transmission is to match both the symmetry of modes and their wave numbers in the straight waveguide and the bend[4]. Fig. 3(a) and 3(b) show the energy distribution in the bends at λ =3.3 μm. The scattering at the bend corner has been efficiently alleviated. The transmittance in bend waveguide at λ = 3.3μm is 85% compared to normal straight waveguide.

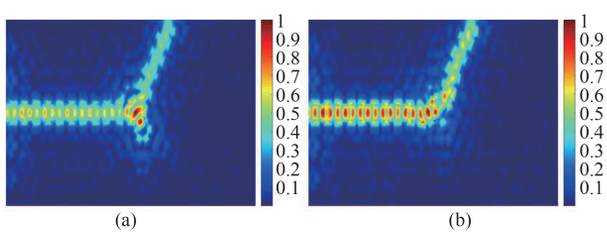

Fig. 3 The energy distribution of (a) the normal bend and (b) the optimized bend.
图3 未优化的弯曲波导(a)和优化后的弯曲波导(b)的能量分布

We can design a cavity by removing or adjusting some holes around a single point. Resonant phenomena in cavities are dependent on the precise geometric properties, such as size and shape. To excite the whispering gallery mode (WGM)[16], we remove the central air hole and reduce the radius of the border holes in the cavity which is denoted as R_c. Such bound modes are guided by means of repeated reflections. After infinite repetitions, absorption, scattering, and material dispersion could be neglected. The structure schemes diagram and energy distribution of the hexapole mode are shown in Fig. 4(a). Due to the hexagonally symmetric WGM field distribution, the phases of adjacent lobes are opposite to each other, so destructive interference occurs and decreases the horizontal radiation. Near the resonant frequency, light from the input waveguide can couple into the cavity, and the cavity in turn can couple into the output waveguide efficiently when $Q_v = Q_h$ is obtained[17], where Q_v is vertical quality factor representing the emission phenomena occurring between the

cavities and free space, and Q_h is horizontal quality factor representing the trapping phenomena occurring between the waveguides and the cavities. The total quality factor Q for a coupled cavity can be written as $Q^{-1} = Q_h^{-1} + Q_v^{-1}$. The expected high quality factor is deduced by the decaying signal in the simulation, because the electromagnetic fields cannot completely decay in the simulation in a reasonably time. The largest Q ~1.2×10^3 is obtained when R_c is 200nm. The cavity works as a WGM cavity, and the resonant peak is dependent on the cavity diameter $D = m\lambda/2n_{eff}$, where m is the order of peaks. The desirable resonant frequency could be reached by shifting the border holes to change the diameter of the cavity.

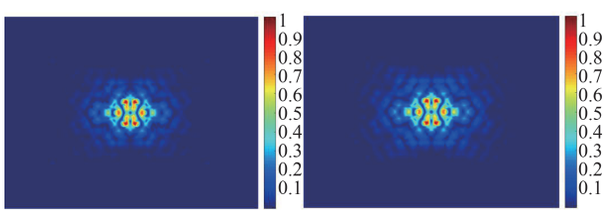

Fig. 4　The energy distribution of (a) the original cavity and (b) the benzene perturbed cavity.
图4　原始腔(a)和苯注入腔(b)的能量分布

The six nearest-neighbor holes in each cavity are pushed 49, 55, 61 and 67nm (denoted as S_i, i = 1, 2, 3 and 4) away from the cavity center to reach the resonant wavelength λ = 3.29, 3.30, 3.31 and 3.32μm, respectively. When the direct reflected light and the light decaying backwards from the cavity cancel exactly by destructive interference, the energy in the cavity decays into the two waveguides at equal rates and the transmission reaches maximum value. The transmission spectrum of the device is depicted in Fig. 5. The transmittance in the channel with center wavelength at λ = 3.30μm is 0.386 and the nonuniformity of transmittance across the four channels is less than 0.022 (i.e. 0.25dB). Quality factors Q is calculated using 3D-FDTD method and listed in Table 1.

Table 1　Resonant wavelengths and quality factor versus Si
表1　共振波长和品质因子与孔位移的对应表

S_i(nm)	Wavelength(nm)	Quality Factor
49	3290.6	1390.87
55	3300.02	1335.04
61	3311.41	1245.75
67	3320	1189.5

The device works as a sensor for solutions with different chemical compositions and concentrations, since the resonant wavelength is sensitive to the refractive index of surrounding environment. We choose the mixture of carbon tetrachloride and benzene as the testing solutions, with the refractive index changing from1.4607

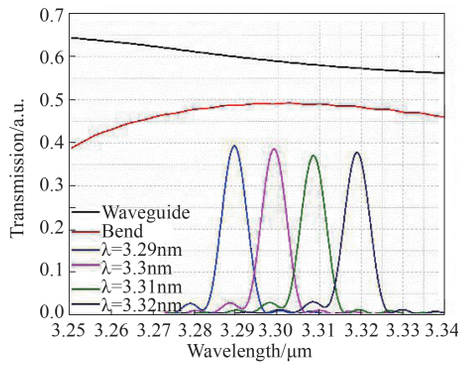

Fig. 5　The transmission spectrum of the bus waveguide (black line), the bend waveguide (red line) and four channels of the sensor
图5　传感器的主波导(黑线)、弯曲波导(红线)和四通道的透射谱

(corresponding to pure carbon tetrachloride) to 1.5012 (corresponding to pure benzene). As shown in Fig. 6 (a), the resonant wavelength of the sensor (center wavelength λ = 3.3μm in air) in different solutions shifts from 3.3772 μm (in carbon tetrachloride solution) to 3.3856 μm (in benzene solution). The linear fits of four channels of the sensor (with center wavelength λ = 3.29, 3.30, 3.31 and 3.32μm in air) between changes of resonant wavelength and changes of concentration are shown in Fig. 6(b). The sensitivity of a sensor is defined as the rate of resonant wavelength shifts with respect to the change in the refractive index, with the corresponding unit of nm/RIU. The sensitivity is calculated as 209.2nm /RIU. This linear red-shift could be explained as the perturbation theory for linear Hermitian eigenproblem. The kernel of the Maxwell equations for a harmonic mode in a mixed dielectric medium is a differential equation for electric field $\mathbf{E}(\mathbf{r})$, given by:

$$\nabla \times \nabla \times \mathbf{E}(\mathbf{r}) = (\omega/c)^2 \varepsilon(\mathbf{r})\mathbf{E}(\mathbf{r}) \quad , \quad (1)$$

By applying the perturbation procedure to equation (1), we obtain a formula for the frequency shift $\Delta\omega$ that results from a small perturbation $\Delta\varepsilon$ of the dielectric function[18]:

$$\Delta\omega = -(\omega/2)\cdot \left(\int d^3r \Delta\varepsilon(\mathbf{r})|\boldsymbol{E}(\mathbf{r})|^2\right) / \left(\int d^3r \varepsilon(\mathbf{r})|\boldsymbol{E}(\mathbf{r})|^2\right) + o(\Delta\varepsilon^2) \quad , \quad (2)$$

In this equation, ω and $\mathbf{E}(\mathbf{r})$ are the frequency and the mode profile for the perfectly linear and unperturbed dielectric function ε. Consider the case of the holes with a refractive index $n = \varepsilon^{1/2}$, in which the index is perturbed in some regions by an amount Δn. The volume integral in the numerator of equation (2) has nonzero contributions only from the perturbed regions. The fractional change in frequency is equal to the fractional change in index multiplied by fraction of the electric-field energy inside the perturbed regions:

$$\Delta\omega/\omega = -F \cdot \Delta n/n \quad , \quad (3)$$

F is a sensitivity function related to the mode profile for the dielectric function ε, and it is a constant since the

change of the mode profile is negligible in this case shown in Fig. 4(b). The change is proportional to the analyte concentration and represents quantitative information about the concentration of the chemical.

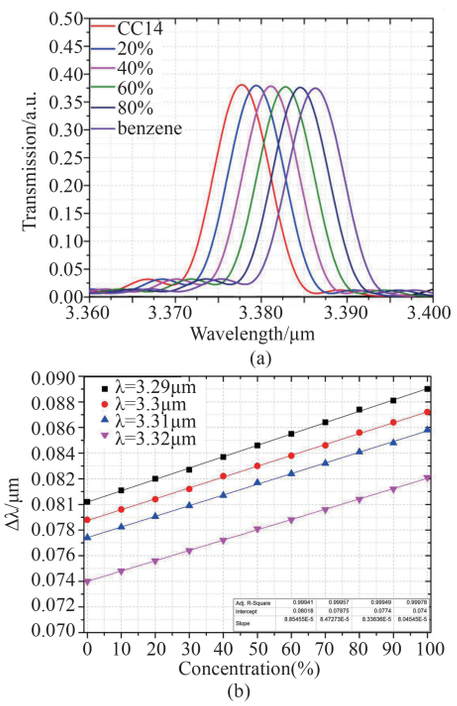

Fig. 6 (a) The shifts in the resonant wavelength of the sensor in pure CCl_4 solutions, pure benzene solutions and mixture of these solutions with different concentrations, (b) The linear fits of four channels of the sensor (with center wavelength λ = 3.29, 3.30, 3.31 and 3.32μm in air) between changes of resonant wavelength and changes of concentration

图6 (a) 传感器在纯四氯化碳溶液、纯苯溶液与四氯化碳和苯的不同浓度混合溶液中的共振波长偏移; (b)四通道传感器(空气中的中心波长为3.29, 3.30, 3.31和3.32μm)的共振波长偏移量与浓度的线性拟合曲线

The previously reported PhC sensors have achieved sensitivities of 363.8 nm/RIU[19], 396 nm/RIU[20], 460 nm/RIU[21-22], 500 nm/RIU[1], higher than the sensitivity of our sensors. However, these sensors have only one channel. A reported multichannel PhC sensor[23] is able to detect four different analytes (with refractive index n= 2.25, 2, 1.75 and 1.5) in four channels, respectively. But this sensor is unable to detect the change of the concentration of analytes (with minor change of refractive index) thus no sensitivity data is shown in this work, which limits the practical application. Besides, the nonuniformity of transmission across the four-channel device in this work is rather large, with the transmittance of four channels ranging from 35% to 95%. In our work, we have achieved a four-channel sensor, which is able to detect the concentration change of mixture of carbon tetrachloride and benzene solutions with a sensitivity of 209.2nm/RIU. And the nonuniformity of transmittance across the four channels in our work is very small, less than 0.022(i.e. 0.25dB).

2 Potential Fabrication and Application

The fabrication of the proposed silicon PhC sensor can be realized on an SOI platform using elelctron beam lithography (EBL) and inductively-coupled plasma (ICP) dry eching which includes the following steps. First, SOI wafer with appropriate top-silicon-thickness should be chosed. Then, electron-beam resist (eg, ZEP520) is spin coated on top of an SOI wafer. Then after exposure to electron beam, the developing and fixing steps are carried out. After that, ICP etching in a gas environment of SF6 and C4F8 is used to form the air holes in PhC sensor. Finally, by removing the resist, the fabrication of PhC sensors is completed. As for the mass production in the future, EBL is replaced by ultra-violet (UV) lithography. First, a mask is fabricated according to the design parameters. Then, using UV lithography technique and the folloing ICP etching technique, thousands of PhC sensors are fabricated on an SOI wafer. Finally, slicing, encapsulation and testing of PhC sensors are carried out.

Standard CMOS process can introduce variations to hole size because of optical proximity effects. The variations in hole size can be considered as deviations from the designed lattice, affecting out-of-plane loss and the photon lifetime of the cavity. Different hole radius, ranging from 374 nm to 394 nm, are simulated to evaluate the tolerance of the sensor, and the results are listed in Table 2. These simulations verify that the sensitivity function is stable with a level about 200nm/RIU though resonant wavelength has shifted as expected. The stability of the sensitivity function can be explained by the unchanged energy distribution of the hexapole whispering gallery mode and quality factor of the sensor. The tolerance of the sensor is large enough to be fabricated by deep UV lithograph for the batch production nowadays.

Table 2 Resonant wavelengths and sensitivity function versus R

表2 共振波长、品质因子和灵敏度与孔半径的对应表

R(nm)	λ(nm)	Q	F(nm/RIU)
374	3343.14	1 404.81	203.7
379	3323.79	1 204.23	209.9
384	3300.02	1 335.04	209.2
389	3280.28	1 220.02	209.9
394	3257.9	1 059.84	209.9

Before the successful application to label-free environmental monitoring and biomedical detection, further work should be done. In this work, we use mixture of carbon tetrachloride and benzene solutions as an example. We need to broaden the working waveband in order to detect more kinds of chemical compounds and molecules. Furthermore, sensitivity should be raised to detect minor change of concentration. In addition, integration of sensors with sources and analyzers are necessary, which includes broadband mid-IR source, polarizer, input fiber, PhC sensor, output fiber, optical spectrum an-

alyzer. Finally, reliability and portability should be considered in future applications.

3 Conclusion

We have proposed a four-channel SOI based 2-D photonic crystal optical sensor suitable for label-free sensing. First, our simulation shows a transmission of 60% for the linear defect waveguide (i. e. the bus waveguide) at λ = 3. 3 μm. Second, we have designed cavities with hexagonally symmetric WGM field distribution reaching a quality factor of about 1.2×10^3. And then, the output bend waveguide is optimized to obtain 85% transmission compared to normal straight waveguide. Finally, the nonuniformity of transmittance across the four-channel device is less than 0. 25 dB, and a sensitivity of 209. 2 nm /RIU is presented. The sensitivity function remains stable when the hole diameter varies ±10 nm. This sensor has potential applications in nanophotonic label-free environmental monitoring and biomedical detection.

Acknowledgment

This work is supported by the Shanghai Sailing Program (No. 18YF1428200, No. 18YF1428100).

References

[1] M. Turduev, I. H. Giden, C. Babayiğit, *et al*. Mid-infrared t-shaped photonic crystal waveguide for optical refractive index sensing [J]. *Sensors & Actuators B Chemical*, 2017, **245**: 765-773.
[2] J. E. Baker, R. Sriram, and B. L. Miller, Recognition-mediated particle detection under microfluidic flow with waveguide-coupled 2D photonic crystals: towards integrated photonic virus detectors [J]. *Lab on A Chip*, 2017, **17**(9): 1570-1577.
[3] P. T. Lin, V. Singh, J. Hu, K. Richardson, *et al*. Mid-infrared chemical sensors on-a-chip using air-clad pedestal silicon waveguides [C]. Lab on A Chip, 2013, **13**(11): 2161-2166.
[4] R. A. Soref, S. J. Emelett, and W. R. Buchwald, Silicon waveguided components for the long-wave infrared region [J]. *Journal of Optics A Pure & Applied Optics*, 2006, **8**(10): 840-848.
[5] A. Y. Petrov, and M. Eich, Zero dispersion at small group velocities in photonic crystal waveguides [J]. *Applied Physics Letters*, 2004, **85**(21): 4866-4868.
[6] Y. Akahane, T. Asano, B. S. Song, *et al*. High-Q photonic nanocavity in a two-dimensional photonic crystal [J]. *Nature*, 2003, **425**(6961): 944-947.
[7] B. S. Song, S. Noda, T. Asano, *et al*. Ultra-high-Q photonic double- heterostructure nanocavity [J]. *Nature Materials*, 2005, **4**(3): 207-210.
[8] A. Mekis, J. C. Chen, I. I. Kurland, *et al*. High transmission through sharp bends in photonic crystal waveguides [J]. *Physical Review Letters*, 1996, **77**(18): 3787-3790.
[9] L. Frandsen, A. Harpøth, P. Borel, *et al*. Broadband photonic crystal waveguide 60° bend obtained utilizing topology optimization [J]. *Optics Express*, 2004, **12**(24): 5916-5921.
[10] S. H. Fan, S. G. Johnson, J. D. Joannopoulos, *et al*. Waveguide branches in photonic crystals [J], *Journal of the Optical Society of America B*, 2001, **18**(2): 162-165.
[11] G. Manzacca, D. Paciotti, A. Marchese, *et al*. 2D photonic crystal cavity-based WDM multiplexer [J]. *Photonics and Nanostructures-Fundamentals and Applications*, 2007,**5**(4): 164-170.
[12] H. Takano, B. S. Song, T. Asano, *et al*. Highly efficient multi-channel drop filter in a two-dimensional hetero photonic crystal [J]. *Optics Express*, 2006, **14**(8): 3491-3496.
[13] W. Li, X. Zhang, X. Lin, *et al*. Enhanced wavelength sensitivity of the self-collimation superprism effect in photonic crystals via slow light [J]. *Optics Letters*, 2014, **39**(15): 4486-4489.
[14] Z. Zhang, S. Satpathy, Electromagnetic wave propagation in periodic structures: bloch wave solution of maxwell's equations [J]. *Physical Review Letters*, 1990, **65**(21): 2650-2653.
[15] G. Ren, W. H. Zheng, Y. J. Zhang, *et al*. Mode analysis and design of a low-loss photonic crystal 60° waveguide bend [J]. *Journal of Lightwave Technology*, 2008, **26**(13-16): 2215-2218.
[16] H. Y. Ryu, M. Notomi, Y. H. Lee, High-quality-factor and small-mode- volume hexapole modes in photonic-crystal-slab nanocavities [J]. *Applied Physics Letters*,2003, **83**(21): 4294-4296.
[17] S. Fan, P. R. Villeneuve, J. D. Joannopoulos, *et al*. Channel drop filters in photonic crystals [J], *Optics Express*, 1998, **3**(1): 4-11.
[18] J. D. Joannopoulos, S. G. Johnson, J. N. Winn, *et al*. Photonic crystals: molding the flow of light [M]. World Publishing Corporation, 2013, 6-228.
[19] Y. N. Zhang, Y.Zhao Q. Wang, Measurement of methane concentration with cryptophane Einfiltrated photonic crystal microcavity [J]. *Sensors and Actuators B*, 2015, **209**:431 - 437.
[20] H. Kurt, M. N. Erim and N. Erim, Various photonic crystal bio-sensor configurations based on optical surface modes [J]. *Sensors and Actuators B*, 2012, **165**: 68 - 75.
[21] T. Lin, X. W. Zhang, G.Y. Zhou, *et al*. Design of an ultra-compact slotted photonic crystal nanobeam cavity for biosensing [J]. *Journal of the Optical Society of America B*, 2015, **32**(9): 1788-1791.
[22] Y. Liu and H. W. M. Salemink, Photonic crystal-based all-optical on-chip sensor [J]. *Optics Express*, 2012, **20**(18): 19912-19920.
[23] M.J. Yun, Y. Wan, J. Liang, *et al*. Multi-channel biosensor based on photonic crystal waveguide and microcavities [J], *Optik*, 2012, **123**: 1920-1922.